PHYSICAL REVIEW APPLIED **18,** 064023 (2022)

Floquet Engineering Using Pulse Driving in a Diamond Two-Level System Under Large-Amplitude Modulation

Shunsuke Nishimura,[1,*] Kohei M. Itoh,[2] Junko Ishi-Hayase,[2] Kento Sasaki,[1,2] and Kensuke Kobayashi[1,3,4]

[1] *Department of Physics, The University of Tokyo, Bunkyo-ku, Tokyo 113-0033, Japan*
[2] *School of Fundamental Science and Technology, Keio University, Kohoku-ku, Yokohama 223-8522, Japan*
[3] *Institute for Physics of Intelligence, The University of Tokyo, Bunkyo-ku, Tokyo 113-0033, Japan*
[4] *Trans-scale Quantum Science Institute, The University of Tokyo, Bunkyo-ku, Tokyo 113-0033, Japan*

(Received 26 April 2022; revised 12 September 2022; accepted 2 November 2022; published 8 December 2022)

The nitrogen-vacancy center (NVC) in a diamond is a promising platform for Floquet engineering. Using the synchronized readout, we investigate the NVC's Floquet state driven by the Carr-Purcell sequence in a large-amplitude ac magnetic field. We observe the dynamics represented as Bessel functions up to 211th order in a systematic and quantitative agreement with the theoretical model. Furthermore, numerical calculations show that the effect of finite pulse duration and error limits the modulation amplitude available for Floquet engineering. This work provides an approach to precisely investigate Floquet engineering, showing the extendable range of modulation amplitude for two-level systems.

DOI: 10.1103/PhysRevApplied.18.064023

I. INTRODUCTION

Floquet theory gives a general formalism for the dynamics of quantum systems subject to periodic driving [1,2]. Recently, utilizations of various periodically driven quantum dynamics as Floquet engineering have been attracting keen attention [3–9]. A thorough investigation of the states produced by diverse periodic drivings is essential for further development. In this context, Floquet engineering using pulse driving has aroused interest as a stage for Hamiltonian engineering [10,11] as well as from perspectives such as discrete-time crystal physics [12–16] and quantum sensing [17–19].

One matter of fundamental interest in Floquet engineering is the fidelity of an experimental system to the physical model under a large-amplitude periodic modulation [20]. The higher-order oscillatory response often appears nonlinearly in this regime, hindering quantitative interpretation. Many researchers have reported the peculiar dynamics in such a large-amplitude regime, for example, Rabi oscillations [21–26], multifrequency absorption [27], Landau-Zener interferometry [28–30], the Carr-Purcell (CP) sequence [31,32], and cavity couplings [33–37]. However, it is still unknown to what extent higher-order nonlinear responses in such a regime can be accurately understood beyond qualitative observations.

In this paper, we focus on a two-level system in a diamond nitrogen-vacancy center (NVC) driven by the CP sequence to enter the Floquet regime. We use ac magnetometry, where an ac magnetic field is applied to a single NVC [17,38–40] driven by the CP sequence, as a test platform of Floquet engineering. Adopting the synchronized readout technique [41–43], we investigate the nonlinear response caused by the phase accumulation in a large-amplitude modulation of the ac magnetic field and, thus, prove that the response obeys the Bessel functions up to as high as 211th order, in accurate agreement with the theory. This work provides a solid foundation for developing pulse-driven Floquet engineering.

This paper is organized as follows. We first define the Floquet picture of pulse drives in Sec. II. In Sec. III, we then describe the principle of extracting the Floquet state by the synchronized readout. After explaining the measurement setup in Sec. IV, we show the experimental results in Sec. V. We discuss the implications and potential applications of the present achievement in Sec. VI, and conclude in Sec. VII.

II. FLOQUET PICTURE

We start with the Floquet picture of the pulse-driven systems in the present study. To realize pulse-driven Floquet engineering, strict periodicity is necessary. For example, the period of the pulse sequence and the other modulations, such as ac field drives, must coincide precisely to realize a periodic Hamiltonian. As a representative of such a pulse-driven Floquet system, we consider the CP sequence with

---

[*] shunsuke.nishimura@phys.s.u-tokyo.ac.jp

© 2022 American Physical Society

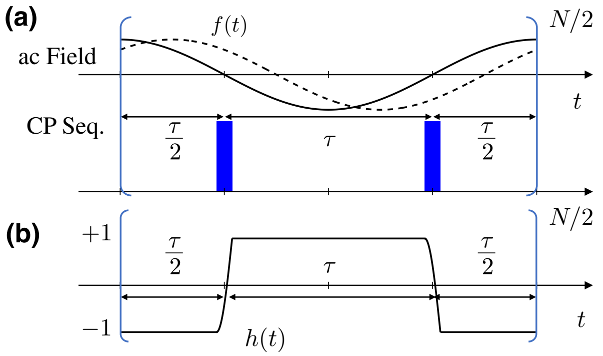

FIG. 1. (a) Diagram of the ac field and the pulse cycle of the CP sequence (CP Seq.). N denotes the total number of pulses. In this case, the number of repetitions equals $N/2$. The dashed curve represents an ac field with different phase. Our method can also apply to an ac field of arbitrary phase, as discussed in Sec. II C. (b) Corresponding modulation function $h(t)$ over time. See Eq. (16).

ac field modulation where the interpulse delay and ac field half-period match, as depicted in Fig. 1(a).

We divide the driving force into two parts, one by the CP sequence and the other by the ac field modulation, as shown in Fig. 1(a). After defining the Floquet state and the Floquet mode in Sec. II A, we extract the time-dependent eigenstates of the CP sequence as a basis in the absence of the ac field in Sec. II B. Then, in Sec. II C, we take the convolution of the time evolution of these eigenstates and the ac field modulation to calculate the total unitary operator in the presence of the ac field drive.

A. Definition

When a Hamiltonian $\hat{H}(t)$ has a periodicity such that $\hat{H}(t) = \hat{H}(t+T)$, the solution $|\Psi_F(t)\rangle$ of the time-dependent Schrödinger equation ($\hbar = 1$),

$$i\frac{\partial}{\partial t}|\Psi_F(t)\rangle = \hat{H}(t)|\Psi_F(t)\rangle, \tag{1}$$

can be described by the Floquet theory. Accordingly, $|\Psi_F(t)\rangle$ can be expressed with periodic states $|\Phi_\alpha(t+T)\rangle = |\Phi_\alpha(t)\rangle$ in the following form:

$$|\Psi_F(t)\rangle = \sum_\alpha c_\alpha e^{i\epsilon_\alpha t}|\Phi_\alpha(t)\rangle, \quad c_\alpha \in \mathbb{C}. \tag{2}$$

Here, we call $|\Psi_F(t)\rangle$ the Floquet state, $|\Phi_\alpha(t)\rangle$ the Floquet mode, and ϵ_α the quasienergy. The Floquet mode and quasienergy are determined by the eigenvalue problem of a time-independent Floquet Hamiltonian $\hat{\mathcal{H}}_\alpha$,

$$\hat{\mathcal{H}}_\alpha = \hat{H}(t) - i\frac{\partial}{\partial t}, \tag{3}$$

$$\hat{\mathcal{H}}_\alpha|\Phi_\alpha(t)\rangle = \epsilon_\alpha|\Phi_\alpha(t)\rangle. \tag{4}$$

The T-periodicity of the Floquet mode straightforwardly explains the stroboscopic response of the Floquet state. Such formalism enables an easy understanding of a periodically driven system.

B. Floquet state driven by CP sequence

We focus on the $m_S = 0$ and -1 states of the NVC in a static magnetic field, which is a two-level system treated in the present experiment [17,38–40]. We express them as $|0\rangle$ and $|1\rangle$, respectively. The spin projection operator $\hat{S}_z$ is then expressed as

$$\hat{S}_z = -|1\rangle\langle 1|. \tag{5}$$

We derive the Floquet state for the CP sequence in the absence of the ac field in this subsection and then show the effect of the ac field in the next subsection. We assume that the microwave pulse is rectangular and resonant to the NVC. The Hamiltonian for the CP sequence in the rotational coordinate system under the rotating wave approximation is given by

$$\hat{H}^{\mathrm{CP}}(t) = \begin{cases} \Omega_R\hat{S}(\phi_1) & \frac{\tau-t_\pi}{2} + 2n\tau \le t < \frac{\tau+t_\pi}{2} + 2n\tau \\ \Omega_R\hat{S}(\phi_2) & \frac{3\tau-t_\pi}{2} + 2n\tau \le t < \frac{3\tau+t_\pi}{2} + 2n\tau \\ 0 & \text{otherwise,} \end{cases}$$
$$\text{for } n = 0, 1, \ldots, N/2 - 1, \tag{6}$$

where $\Omega_R = \pi/t_\pi$ is the Rabi frequency, $\hat{S}(\phi_i) = \frac{1}{2}(e^{i\phi_i}|1\rangle\langle 0| + e^{-i\phi_i}|0\rangle\langle 1|)$, ϕ_i is the pulse phase ($i = 1, 2$), t_π is the π pulse duration, τ is the interpulse delay, and N is the number of π pulses.

The Hamiltonian [Eq. (6)] is modified according to the pulse phase series used in the CP sequence. For technical reasons, we first consider the situation where the pulse duration takes the finite span t_π. Since it has a periodicity of $T = 2\tau$, a quantum state under the Hamiltonian is a Floquet state. When the initial state is $|\psi_0(t=0)\rangle = |0\rangle$, the time evolution in one cycle $t = [0, 2\tau]$ of the CP sequence is obtained as

$$|\psi_0(t)\rangle = \begin{cases} |0\rangle & 0 \le t < \frac{\tau-t_\pi}{2} \\ \hat{U}_p(\phi_1, t, \frac{\tau-t_\pi}{2})|0\rangle & \frac{\tau-t_\pi}{2} \le t < \frac{\tau+t_\pi}{2} \\ -ie^{-i\phi_1}|1\rangle & \frac{\tau+t_\pi}{2} \le t < \frac{3\tau-t_\pi}{2} \\ -ie^{-i\phi_1}\hat{U}_p(\phi_2, t, \frac{3\tau-t_\pi}{2})|1\rangle & \frac{3\tau-t_\pi}{2} \le t < \frac{3\tau+t_\pi}{2} \\ -e^{-i(\phi_1-\phi_2)}|0\rangle & \frac{3\tau+t_\pi}{2} \le t < 2\tau, \end{cases} \tag{7}$$

where $\hat{U}_p(\phi, t_f, t_i)$ represents the pulse operation during $t \in [t_i, t_f]$ with phase ϕ, which is given by

$$\begin{aligned}\hat{U}_p(\phi, t_f, t_i) &= \exp\left[-i\frac{\pi}{t_\pi}(t_f - t_i)\hat{S}(\phi)\right] \\ &= \cos\left[\frac{\pi}{2t_\pi}(t_f - t_i)\right]\mathbf{1} - 2i\sin \\ &\quad \times \left[\frac{\pi}{2t_\pi}(t_f - t_i)\right]\hat{S}(\phi). \end{aligned} \tag{8}$$

The state $|\psi_0(t)\rangle$ is an eigenstate of the Hamiltonian [Eq. (6)], which satisfies Eq. (1), and therefore a Floquet state. Similarly, the state

$$|\psi_1(t)\rangle = (|1\rangle\langle 0| + |0\rangle\langle 1|)\,|\psi_0(t)\rangle\,, \tag{9}$$

which is orthogonal to $|\psi_0(t)\rangle$ is also a Floquet state. These two states are, by nature, normalized and orthogonal to each other. Furthermore, the basis of these two states $|\psi_0(t)\rangle$ and $|\psi_1(t)\rangle$ spans the whole Floquet state represented in Eq. (2).

The global phase offset $\phi_1 - \phi_2 + \pi$ is accumulated to the quantum state every cycle of the CP sequence as in Eq. (7). This phase does not change the observables in this two-level system. Thus, for simplicity, we fix the pulse phase condition to be $\phi_1 - \phi_2 + \pi = 0$. We denote by $|\Phi_0^{\rm CP}(t)\rangle$ and $|\Phi_1^{\rm CP}(t)\rangle$ the special case of $|\psi_0(t)\rangle$ and $|\psi_1(t)\rangle$, respectively, for that condition. Then they satisfy the following periodic conditions:

$$|\Phi_0^{\rm CP}(t+2\tau)\rangle = |\Phi_0^{\rm CP}(t)\rangle\,, \tag{10}$$

$$|\Phi_1^{\rm CP}(t+2\tau)\rangle = |\Phi_1^{\rm CP}(t)\rangle\,. \tag{11}$$

These states are Floquet modes defined in Eq. (2) with quasienergy $\epsilon_\alpha^{\rm CP} = 0$. With these Floquet modes, the Floquet state $|\Psi_F(t)\rangle$ is expressed by using appropriate coefficients c_0' and c_1' such that

$$|\Psi_F(t)\rangle = c_0'\,|\Phi_0^{\rm CP}(t)\rangle + c_1'\,|\Phi_1^{\rm CP}(t)\rangle\,. \tag{12}$$

Now, without losing the essence of the Floquet picture, we can set the π pulse duration $t_\pi \to 0$. The CP pulse Hamiltonian Eq. (6) within one period $[0, 2\tau]$ can be rewritten using the Dirac delta $\delta(t)$ as

$$\hat{H}^{\rm CP}(t) = \pi\delta(t - \tau/2)\hat{S}(\phi_1) + \pi\delta(t - 3\tau/2)\hat{S}(\phi_2). \tag{13}$$

Accordingly, the Floquet modes of the CP sequence are represented as the eigenstates of $\hat{H}^{\rm CP}(t)$ such that

$$|\Phi_0^{\rm CP}(t)\rangle = \frac{1-h(t)}{2}\,|0\rangle + \frac{1+h(t)}{2}\,|1\rangle\,, \tag{14}$$

$$|\Phi_1^{\rm CP}(t)\rangle = \frac{1+h(t)}{2}\,|0\rangle + \frac{1-h(t)}{2}\,|1\rangle\,, \tag{15}$$

where $h(t)$ is the modulation function

$$h(t) = \begin{cases} -1 & 0 < t < \frac{\tau}{2}, \quad \frac{3\tau}{2} < t < 2\tau \\ 1 & \frac{\tau}{2} < t < \frac{3\tau}{2} \end{cases} \tag{16}$$

which is depicted in Fig. 1(b).

Equations (7) and (9) tell us that since the pulse phases, ϕ_1 and ϕ_2, do not affect the overall dynamics of the Floquet state other than the global phase, we can choose them arbitrarily. Thus, in our experiment, we employ a pulse cycle containing multiple phases for robust operation as detailed in Sec. IV C.

C. Precession of the Floquet state driven by CP sequence in the ac magnetic field

We consider the case where an arbitrary ac magnetic field $f(t)$ is applied in the direction of the symmetry axis of the NVC. Generally, a periodic function $f(t)$ with a period $T = 2\tau$ can be expanded in the Fourier series as

$$f(t) = a_0 + \sum_{k=1}^{\infty}[a_k\cos(k\omega t) + b_k\sin(k\omega t)]\,, \tag{17}$$

where $\omega = \pi/\tau$. A Hamiltonian under the ac magnetic field is given in the Hilbert space that the spin operator basis spans:

$$\hat{H}^{\rm ac}(t) = f(t)\hat{S}_z = -f(t)\,|1\rangle\langle 1|\,. \tag{18}$$

The total Hamiltonian $\hat{H}$ for the quantum state driven by the CP sequence in the ac magnetic field is given by

$$\hat{H}(t) = \hat{H}^{\rm ac}(t) + \hat{H}^{\rm CP}(t), \tag{19}$$

which is represented on the same basis.

From here, in order to clarify the effect of the ac magnetic field on the Floquet state, we write down the above Hamiltonian $\hat{H}$ on the basis of the Floquet mode $|\Phi_i(t)^{\rm (CP)}\rangle$, $i = 0, 1$, in Eqs. (14) and (15). We use the following unitary transformation $\hat{U}_t(t)$ to represent the frame change $|i\rangle \to |\Phi_i(t)^{\rm CP}\rangle$:

$$\hat{U}_t(t) = |\Phi_0^{\rm CP}(t)\rangle\langle 0| + |\Phi_1^{\rm CP}(t)\rangle\langle 1|\,. \tag{20}$$

This unitary transformation represents the driving of the spin state by $\hat{H}^{\rm CP}(t)$. Since $|\Phi_i^{\rm CP}(t)\rangle$ are orthonormal eigenstates of $\hat{H}^{\rm CP}(t)$ [Eq. (13)] that satisfy the time-dependent Shrödinger equation [Eq. (1)], the identity

$i\frac{\partial \hat{U}_t}{\partial t}(t) = \hat{H}^{\mathrm{CP}}(t)\hat{U}_t(t)$ holds. Then we find that

$$i\hat{U}_t^{\dagger}(t)\frac{\partial \hat{U}_t}{\partial t}(t) = \hat{H}^{\mathrm{CP}}(t). \tag{21}$$

Thus, in this frame, the total Hamiltonian $\breve{H}(t)$ is given by

$$\begin{aligned}\breve{H}(t) &= \hat{U}_t^{\dagger}(t)\hat{H}(t)\hat{U}_t(t) - i\hat{U}_t^{\dagger}(t)\frac{\partial \hat{U}_t}{\partial t}(t) \\ &= -f(t)\frac{1+h(t)}{2}\left|0\right\rangle\left\langle 0\right| - f(t)\frac{1-h(t)}{2}\left|1\right\rangle\left\langle 1\right|.\end{aligned} \tag{22}$$

In the above, we utilize the following identities:

$$\left(\frac{1\pm h}{2}\right)^2 = \frac{1\pm h}{2}, \quad \left(\frac{1+h}{2}\right)\left(\frac{1-h}{2}\right) = 0.$$

In the presence of the ac field, the precession frequencies of the two states $\left|0\right\rangle, \left|1\right\rangle$ are given by

$$\xi_0^{\mathrm{CP}}(t) = -f(t)\frac{1+h(t)}{2}, \quad \xi_1^{\mathrm{CP}}(t) = -f(t)\frac{1-h(t)}{2}, \tag{23}$$

respectively. Thus, the phase accumulations during $t = [0, 2\tau]$ that correspond to the quasienergies are calculated as

$$\phi_0 = \int_0^{2\tau} \xi_0^{\mathrm{CP}}(t)dt = -a_0\tau - \sum_{j=0}^{\infty} a_{2j+1}\frac{2(-1)^j}{(2j+1)\omega}, \tag{24}$$

$$\phi_1 = \int_0^{2\tau} \xi_1^{\mathrm{CP}}(t)dt = -a_0\tau + \sum_{j=0}^{\infty} a_{2j+1}\frac{2(-1)^j}{(2j+1)\omega}. \tag{25}$$

Here, we use the symmetry $h(t) = h(2\tau - t)$, the property of convolution $(h * f)(2\tau) = \int_0^{2\tau} h(2\tau - t)f(t)dt$, and the Fourier series of $h(t)$ given by

$$h(t) = \sum_{j=0}^{\infty} \frac{4}{\pi}\frac{(-1)^j}{(2j+1)}\cos[(2j+1)\omega t]. \tag{26}$$

Since $h(t)$ consists only of the odd-order cosine part of the Fourier composition, only the matched components of $f(t)$ [a_{2j+1} in Eq. (17)] contribute to the dynamics, as derived from the property of the convolution. The dynamics $\hat{U}$ in the overall sequence $t = [0, 2\tau \times (N/2)]$ is obtained as

$$\hat{U} = e^{i\phi_0(N/2)}\left|0\right\rangle\left\langle 0\right| + e^{i\phi_1(N/2)}\left|1\right\rangle\left\langle 1\right|, \tag{27}$$

and here

$$\phi_{\mathrm{acq}} = \frac{N}{2}(\phi_1 - \phi_0) = \sum_{j=0}^{\infty} a_{2j+1}\frac{2N(-1)^j}{(2j+1)\omega} \tag{28}$$

is the phase difference between Floquet modes. In the stroboscopic measurement at the end of the CP sequence, the state $\left|0\right\rangle$ ($\left|1\right\rangle$) is experimentally indistinguishable from the state $\left|\Phi_0^{\mathrm{CP}}(t)\right\rangle$ ($\left|\Phi_1^{\mathrm{CP}}(t)\right\rangle$). Thus, the treatment that exploits the frame change $\left|i\right\rangle \to \left|\Phi_i^{\mathrm{CP}}(t)\right\rangle$ can be used to describe the Floquet state of the pulsed drives.

The Floquet state dynamics is explained by the convolution of the modulation function $h(t)$ and the target ac field $f(t)$. The CP sequence can be understood as engineering to extract only the cosine of the odd harmonic components of $f(t)$ as in Eq. (25). By designing the modulation function $h(t)$ by adjusting τ appropriately, we can extract any frequency components of the ac field.

III. SYNCHRONIZED READOUT

We have obtained the phase dynamics of the Floquet state driven by the CP sequence in the ac magnetic field. The dynamics is reflected in the phase acquisition ϕ_{acq}. We next formulate the principle of retrieving the Floquet state by the so-called synchronized readout, which we focus on in this study.

A. Phase dynamics measurement of a Floquet state by the synchronized readout

We use the initial state

$$\left|\Psi_F(t=0)\right\rangle = (\left|0\right\rangle - i\left|1\right\rangle)/\sqrt{2} \tag{29}$$

to interferometrically measure the difference of the phase acquisition in the Floquet modes [see Eq. (12)]. Setting the phase of the readout $\pi/2$ pulse to $\phi = \pi/2$, the probability of detecting the quantum state as $\left|0\right\rangle$ is obtained as

$$P_0 = \frac{1 + \sin\phi_{\mathrm{acq}}}{2}. \tag{30}$$

The phase accumulation is experimentally accessible by probing P_0.

We systematically investigate ϕ_{acq} by using the synchronized readout technique. As shown in Fig. 2, this technique repeats the CP sequence at a time interval of t_L. We redefine the time origin t as the timing of the first CP sequence of the synchronized readout; the start time of the mth CP sequence ($m = 1, 2, 3, \ldots$) is $t_m = (m-1)t_L$. The time

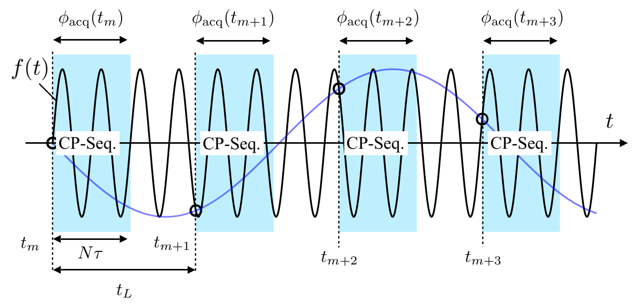

FIG. 2. Schematic of the synchronized readout. The blue-shaded blocks marked “CP-Seq.” represent the sequence shown in Fig. 1(a). The blue line represents the systematic ac field phase shift in each CP sequence. The period of this blue-line modulation is determined by both the period of the ac field (2τ) and the time interval t_L of the synchronized readout, and is obtained from the undersampling condition (see Appendix A).

shift in the CP sequences causes a systematic phase shift to the ac field [Eq. (17)] such that

$$f\,(t+t_m) = a_0 + \sum_{k=1}^{\infty}[a_k\cos(k\omega t_m) + b_k\sin(k\omega t_m)] \times\cos(k\omega t) + [-a_k\sin(k\omega t_m) + b_k\cos(k\omega t_m)] \times\sin(k\omega t). \tag{31}$$

Then $\phi_{\rm acq}(t_m)$ in the mth CP sequence can be derived from Eq. (28) and the Fourier expansion of $f\,(t)$ [Eq. (17)] as follows:

$$\phi_{\rm acq}(t_m) = \sum_{j=0}^{\infty}\frac{2N(-1)^j}{(2j+1)\omega}\{a_{2j+1}\cos[(2j+1)\omega t_m] + b_{2j+1}\sin[(2j+1)\omega t_m]\}. \tag{32}$$

The Fourier series for t_m of $\phi_{\rm acq}(t_m)$ contains all odd harmonic components of $f\,(t)$. We can obtain each odd harmonic component of $f\,(t)$ as the spectrum of the time-series readout result $\{P_0(t_m)\}$.

B. Fourier decomposition to extract experimental signal

Our experiment observes the dynamics in the simplest sinusoidal ac magnetic field. It corresponds to the case where all the Fourier series components except for $k=1$ in Eqs. (17) and (31) are zero, that is,

$$\begin{aligned} f\,(t) &= \gamma b_{\rm ac}\cos(\omega_{\rm ac}t+\phi_{\rm ac}) \\ &= \gamma b_{\rm ac}\cos(\phi_{\rm ac})\cos(\omega_{\rm ac}t) - \gamma b_{\rm ac}\sin(\phi_{\rm ac})\sin(\omega_{\rm ac}t), \end{aligned} \tag{33}$$

where $b_{\rm ac}$, $\omega_{\rm ac}$ ($=\pi/\tau$), and $\phi_{\rm ac}$ are the amplitude, the frequency, and the phase of the ac field, respectively, and $\gamma = 2\pi\times 28$ rad GHz/T is the gyromagnetic ratio. According to Eq. (32), the phase acquisition at the mth CP sequence is obtained as

$$\begin{aligned} \phi_{\rm acq}(t_m) &= \frac{2N\gamma b_{\rm ac}}{\omega_{\rm ac}}[\cos\phi_{\rm ac}\cos(\omega_{\rm ac}t_m) - \sin\phi_{\rm ac}\sin(\omega_{\rm ac}t_m)] \\ &= \frac{2N\gamma b_{\rm ac}}{\omega_{\rm ac}}\cos(\omega_{\rm ac}t_m+\phi_{\rm ac}). \end{aligned} \tag{34}$$

The signal at the mth readout is obtained as

$$\begin{aligned} P_0(t_m) &= \frac{1}{2} + \frac{1}{2}\sin\left[\frac{2N\gamma b_{\rm ac}}{\omega_{\rm ac}}\cos(\omega_{\rm ac}t_m+\phi_{\rm ac})\right] \\ &= \frac{1}{2} + \frac{1}{2}{\rm Im}\left[\exp\left(i\frac{2N\gamma b_{\rm ac}}{\omega_{\rm ac}}\cos(\omega_{\rm ac}t_m+\phi_{\rm ac})\right)\right]. \end{aligned} \tag{35}$$

The Fourier series expansion of the signal for t_m is obtained as

$$P_0(t_m) = \frac{1}{2} + \sum_{k:{\rm odd}} A_k\cos(k\omega_{\rm ac}t_m+\phi_k), \tag{36}$$

$$A_k = J_k\left(2N\frac{\gamma b_{\rm ac}}{\omega_{\rm ac}}\right), \tag{37}$$

$$\phi_k = k\left(\frac{N\pi}{2}+\phi_{\rm ac}-\frac{\pi}{2}\right)-\frac{\pi}{2}, \tag{38}$$

where J_k is a Bessel function of the first kind of kth order. Here, we use the Jacobi-Anger identity

$$e^{ia\cos\varphi} = \sum_{n\in\mathbb{Z}} i^n J_n(a)e^{in\varphi}. \tag{39}$$

The frequency resolution of the discrete Fourier transformation (DFT) spectrum can be set arbitrarily by the inverse of the total duration of the synchronized readout. Thus, with high accuracy, we can investigate the response dependent on the amplitude and phase of the ac field. According to Eq. (37), higher-order Bessel functions take a nonzero value and oscillate when the magnetic field amplitude increases. For a sufficiently weak magnetic fields, A_k behaves linearly with respect to the changes in $b_{\rm ac}$. The threshold above which the response is no longer regarded as linear should be

$$b_{\rm ac} \approx \frac{\pi}{2}\frac{\omega_{\rm ac}}{2N\gamma}. \tag{40}$$

Our primary concern in the present work is to determine the degree to which the ac field amplitude is consistent with the DFT amplitude given by Eq. (37) as a crucial test of the robustness of this Floquet state against large-amplitude modulation.

IV. EXPERIMENTS

This section describes our experimental condition. We measure a single NVC in a diamond substrate (of electrical grade from Element Six) using a homemade confocal system [44].

A. Setups

Figure 3(a) is the schematic of our experimental setup. We apply a static bias magnetic field of around 30 mT by a neodymium magnet beneath the diamond [not shown in Fig. 3(a)] to lift the spin degeneracy of the energy levels. For the generation of a microwave field to control the NVC, we use a copper stripline of approximately 1 μm thick and 200 μm wide fabricated right on the surface of the diamond using an electron-beam deposition. The microwave pulse waveform is generated by in-phase and quadrature modulation of a vector signal generator with an arbitrary waveform generator, amplified by a typically +45 dB microwave amplifier (Mini-circuit ZHL-16W-43S+) and passed through the stripline. The ac external magnetic field is generated by the solenoid coil situated beneath the diamond, as presented in Fig. 3(a). A function generator and typically +43 dB amplifier (Mini-circuit LZY-22+) to generate a sinusoidal wave voltage at 500.1 kHz are connected to the coil. The function generator is triggered by the same arbitrary waveform generator that synchronizes the phase at the start of the synchronized readout. The clocks on all instruments are locked by a rubidium clock.

B. Calibration

We check the linearity between the applied voltage amplitude of the function generator and the resulting field amplitude b_{ac} before the main experiment. We measure b_{ac} with the ac magnetometry by sweeping the interpulse delay τ of the ordinary CP sequence [31]. We set the π pulse duration to $t_\pi = 19.8$ ns and the number of π pulses to $N = 16$ for the CP sequence. Only in this measurement do we randomize the phase of the ac magnetic field and deviate the period of the pulse sequence from that of the ac field. The spectra obtained for applied voltage amplitude $0.0, 2.0, 5.0, 7.0, 10.0, 15.0$, and 20.0 $\mathrm{mV_{p.p.}}$ are shown in Fig. 3(b). The horizontal axis is the detection frequency $1/2\tau$, and the vertical axis is the transition probability of the NVC. As the voltage is increased, a signal appears near 500.1 kHz. We fit the data with the following analytical model [45]:

$$P_0 = \frac{1}{2}\left(1 - J_0(|W_a|\gamma b_{\mathrm{ac}} N\tau)\right), \tag{41}$$

$$W_a = \frac{\sin(\omega_{\mathrm{ac}} N\tau/2)}{\omega_{\mathrm{ac}} N\tau/2}\left(1 - \frac{1}{\cos(\omega_{\mathrm{ac}}\tau/2)}\right), \tag{42}$$

where J_0 is the zeroth-order Bessel function. The fitted spectra are shown as the solid lines in Fig. 3(b). The model nicely explains the experimental data for all the input voltage amplitudes. Note that the small difference between the experimental data and the fitting at around 300 kHz is due to the effect of ^{13}C nuclear spins near the present NVC. In order to obtain b_{ac} accurately, we exclude this region from the fitting. The relationship obtained between the applied voltage and the generated magnetic field amplitude is shown in Fig. 3(c). We get excellent linearity, yielding a conversion factor of 0.381 ± 0.004 $\mu\mathrm{T/mV_{p.p.}}$.

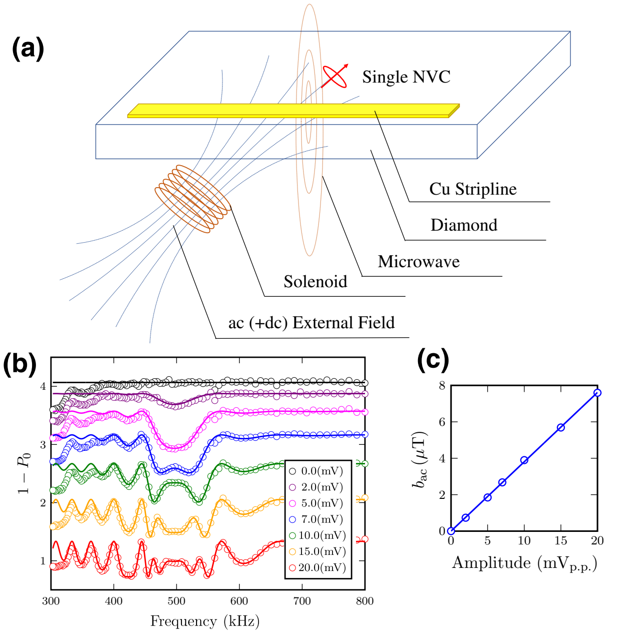

FIG. 3. (a) Schematic of our experimental setup. (b) Alternating current (ac) magnetometry using CP sequence. The target ac magnetic field frequency is 500.1 kHz. For clarity, the data of each condition are shifted vertically. (c) The relation between input voltage amplitude and ac field amplitude obtained from the fitting of (b).

C. Protocol

Throughout our experiment, we use the same NVC and set the duration and the number of π pulses to the same values as we use in the prerequisite experiment ($t_\pi = 19.8$ ns and $N = 16$, respectively). In this situation, we set the interpulse delay to $\tau = \pi/\omega_{\mathrm{ac}}$ to realize the Floquet state of $N/2 = 8$ cycles of the CP sequence. We observe the response as formulated in Sec. II B. The ac magnetic field of $\omega_{\mathrm{ac}} = 2\pi \times 500.1$ kHz is generated by applying an ac voltage to the solenoid. By increasing the voltage amplitude from 0.4 $\mathrm{mV_{p.p.}}$ to 300 $\mathrm{mV_{p.p.}}$, an ac magnetic field with an amplitude up to about 120 μT is produced, which is far beyond the small-amplitude regime, $b_{\mathrm{ac}} \approx (\omega_{\mathrm{ac}}/2N\gamma) \times (\pi/2) = 877$ nT [Eq. (40)]. We set the period of the synchronized readout as $t_L = 20.0$ μs and measure 335.5 s with fivefold integration. In this condition, kth harmonics should appear at a DFT frequency of

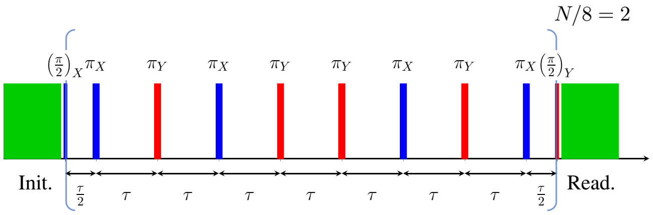

FIG. 4. XY8 pulse sequence used in our experiment ($N = 16$).

$k \times 100$ Hz (see Appendix A). As mentioned in Sec. II, the overall dynamics does not depend on the phase cycles of pulse operations. We thus set the phase cycle as XY8 to reduce experimental pulse error. Figure 4 shows the phase cycle we adopt in our experiment.

V. RESULTS

A. DFT spectra at each ac field amplitude

Figure 5(a) shows the DFT spectrum obtained when the voltage amplitude to generate an ac magnetic field is set as small as 2 $\mathrm{mV_{p.p.}}$. A large peak at 100 Hz and a small peak at 300 Hz correspond to the harmonics of $k = 1$ and $k = 3$, respectively. Note that the signal is undersampled due to the time resolution of a finite measurement window (see Appendix A). The absence of peaks higher than $k = 3$ tells us that the ac field amplitude is sufficiently small and the system is in the linear regime. This is a condition similar to those reported in previous studies using the synchronized readout [41–43]. Additionally, we see a peak at 200 Hz smaller than the peak at 300 Hz. This even harmonic is caused by a pulse error (see Appendix C). The present high-frequency resolution achieved by the synchronized readout enables us to detect such a small signal.

B. Harmonic signals depending on field amplitude

We then show the modulation voltage amplitude dependence of the DFT spectra. Figure 5 shows the DFT spectra when voltage amplitudes of 2 $\mathrm{mV_{p.p.}}$, 10 $\mathrm{mV_{p.p.}}$, 50 $\mathrm{mV_{p.p.}}$, 100 $\mathrm{mV_{p.p.}}$, and 300 $\mathrm{mV_{p.p.}}$ are applied. As seen in this figure , odd harmonics appear up to higher orders successively as the amplitude increases. In particular, even a harmonic peak for $k = 211$ is observed in the spectrum for 300 $\mathrm{mV_{p.p.}}$ in Fig. 5(e). Such a higher-order response has not been investigated with such high precision before. A finite offset of about 3000 counts due to photon shot noise is commonly present in all the data in Figure 5.

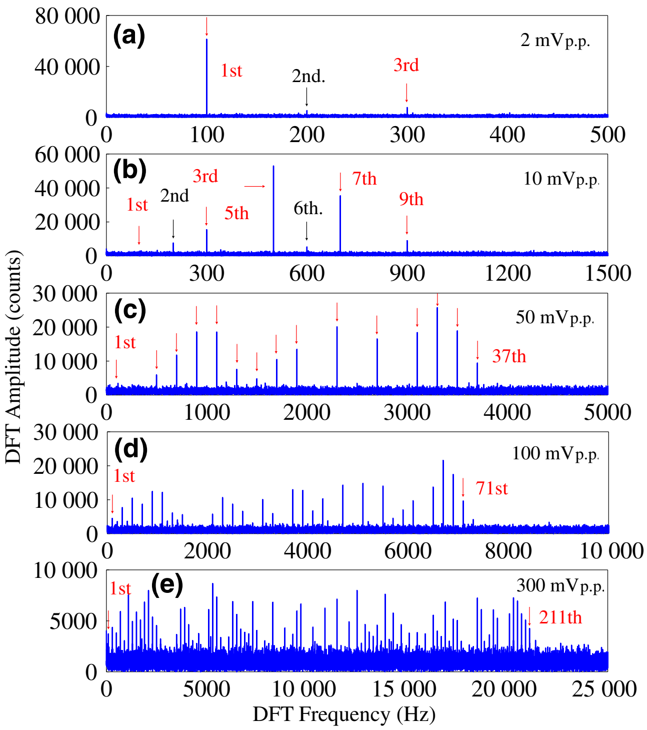

FIG. 5. DFT spectra at several ac voltage amplitudes: (a) 2 $\mathrm{mV_{p.p.}}$; (b) 10 $\mathrm{mV_{p.p.}}$; (c) 50 $\mathrm{mV_{p.p.}}$; (d) 100 $\mathrm{mV_{p.p.}}$; (e) 300 $\mathrm{mV_{p.p.}}$. A finite vertical offset of about 3000 counts due to photon shot noise is commonly present in all the data.

We now quantitatively examine the amplitude of each harmonic by comparing it to the Bessel function [Eq. (37)]. Figure 6 shows the results for the 1st, 11th, 51st, 151st, and 201st harmonics. The blue circles show the DFT amplitudes obtained by fitting the DFT spectra normalized to the state probabilities by the experimentally calibrated NVC's photoluminescence intensity (see Appendix B). The constant offset of about 0.05 present in each figure is an artifact of the peak analysis due to the photon shot noise mentioned above. The solid red lines show the analytical results fitted by Eq. (37), reasonably assuming that the voltage amplitude and ac magnetic field amplitude are proportional and using only the coefficient of the proportionality is used as an estimation parameter. The coefficient obtained is 0.392 $\mu\mathrm{T/mV_{p.p.}}$, almost consistent with that obtained from the prerequisite test (0.381 ± 0.004 $\mu\mathrm{T/mV_{p.p.}}$) in Sec. IV B. The slight deviation (approximately 2.9%) is possibly due to the quasiperiodic distortion observed in the experimental signal in Fig. 6, which will be discussed in the next subsection.

We find that the oscillation period and amplitude of both experimental and theoretical [Eq. (6)] oscillation are in general agreement, even up to higher-order harmonics exceeding 200. These results mean that the Floquet state of the pulse-driven NVC is maintained even in large-amplitude modulation. It is also significant that each DFT amplitude is consistent with theory without any artificial normalization; it indicates that the synchronized readout contributes to a highly quantitative measurement.

The ac field amplitude in the present experiment ranges from 157 nT at minimum to 118 μT at maximum, confirming that our investigation is systematic over a wide amplitude range, from a regime near the linear response to one that is highly nonlinear and nonequilibrium. Although

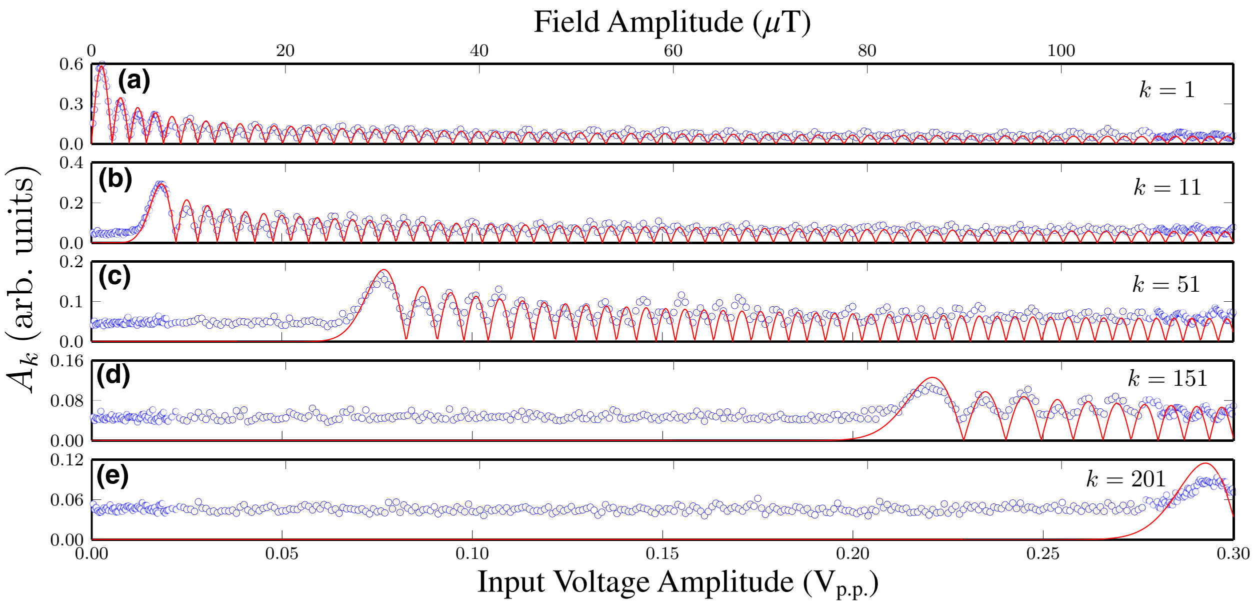

FIG. 6. Input voltage amplitude dependence of the peak amplitude for (a) 1st, (b) 11th, (c) 51st, (d) 151st, and (e) 201st harmonics. The top axis show the magnetic field amplitude estimated from the fitting coefficient 0.392 μT/mV$_{\text{p.p.}}$ (see main text).

similar experiments in previous studies have observed the response to be a Bessel function [46] and the appearance of multiple harmonics [47], we find that the peak amplitudes are quantitatively consistent over a significantly more extensive amplitude range than those. While large-amplitude modulation in different physical phenomena can give dynamics exhibiting Bessel functions [7,27], Bessel functions of as high as 200th order have never been observed experimentally. The synchronized readout for the NVC is relevant in addressing Floquet state dynamics in such a large-amplitude modulation.

C. Comparison between experiments and theoretical calculation

We compare all of the experimentally observed harmonics with the theoretical calculations in terms of the ac field amplitude dependence. Figure 7(a) shows the intensity plot of the experimental result as functions of the field amplitude and the order of harmonics k. Figure 7(b) shows the corresponding $|A_k|$, deduced from Eq. (37). These figures are almost consistent, indicating that Eq. (37) can, in principle, explain all harmonic behaviors observed in this experiment.

A more careful comparison reveals irregular fluctuations in the experimental intensity [Fig. 7(a)], not present in Fig. 7(b). We compare this behavior with a more detailed physical model that includes finite pulse duration and errors. Figures 7(c) and 7(d) show the numerical results for finite pulse duration with and without the duration error of 4% (−0.8 ns), respectively. Both show irregular fluctuations, and in particular the result in Fig. 7(c) agrees very well with the experimental results [Fig. 7(a)]. These observations suggest a slight inevitable pulse error in the experiment. This fact also explains the appearance of the small even-order harmonics in Fig. 5. Such a small pulse error can appear in the rise and fall times of the rectangular pulses used in the CP sequence.

Further numerical calculations show that the bandwidth of the pulse excitation limits the measurable amplitude range. Figures 7(e) and 7(f) show the numerical calculations for $t_\pi = 100$ ns and $t_\pi = 400$ ns, respectively. The respective pulse durations are 5 and 20 times as long as that used in the present experiment ($t_\pi = 19.8$ ns). As shown in Figs. 7(e) and 7(f), as the pulse duration lengthens, more irregular fluctuations appear, and higher-order harmonics are no longer observable. This is because the bandwidth of the pulse excitation ($1/t_\pi$) gets narrower than the range of the NVC's resonance frequency modulation. We observe that the amplitude of the higher-order harmonics is almost zero in the area where the ac field amplitude is large, that is, larger than that around 80 μT in Fig. 7(e) and around 20 μT in Fig. 7(f). There, the driving force by ac field exceeds the microwave pulse driving and breaks down the pulse-driven Floquet state.

VI. DISCUSSION

We discuss two significant implications of the present result for Floquet engineering. First, based on the above development, we can largely extend the modulation amplitude range available for Floquet engineering, such as quantum sensing [18,19,48–50]. The method demonstrated is advantageous in observing dressed states [48,50–52]

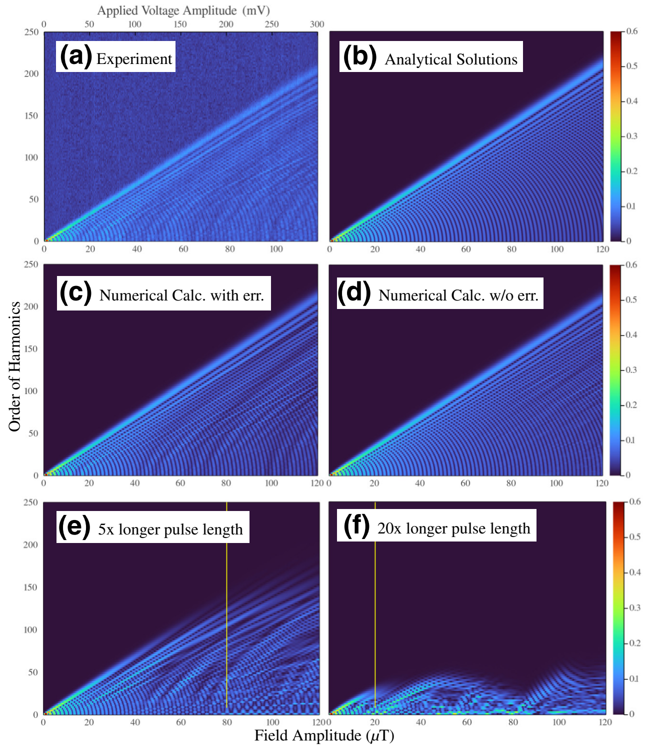

FIG. 7. Two-dimensional intensity plots of the peak amplitude as functions of the ac field amplitude and harmonics k up to 250. The color scale is common for all the panels (a)–(f). (a) Experimental result. (b) Analytical result [Eq. (37)]. (c) Numerical result including finite pulse duration with a duration error of 4% (-0.8 ns). (d) Numerical result including finite pulse duration without duration error. (e) Numerical result for an experiment lasting 5× as long as the present one ($t_\pi = 100$ ns). (f) Numerical result for an experiment lasting 20× as long as the present one ($t_\pi = 400$ ns).

and many-body states formed by interactions with surrounding spins [12,13]. As a system with robust Floquet states, the pulse-driven NVC can also be helpful in evaluating the effects of finite pulse duration and error in general two-level systems [14,53–56]. Second, exploring the non-Hermitian Floquet dynamics is a promising direction. In the present experiment, the CP sequence readout completely initializes the NVC, quenching the Floquet state. Conversely, the synchronized readout with partial initialization or weak measurement of the NVC and surrounding nuclear spins [57,58] would serve as a platform to investigate non-Hermitian Floquet dynamics [16,59].

VII. CONCLUSION

We precisely observed the dynamics of the NVC's Floquet state driven by the CP sequence in large-amplitude modulation as the higher-order harmonics up to 211 by using the synchronized readout technique. We have thus established the relevance of the high precision of the synchronized readout in Floquet engineering. The nonlinear response of the Floquet state to the magnetic field is quantitatively reproduced by numerical simulations, including the effects of finite pulse duration and error. This study further enhances the potential of the NVC as an ideal platform for Floquet engineering.

Finally, we consider potential applications of the present result to quantum sensing. Our experiment has confirmed that multiple peaks sharply change according to the Bessel functions in response to changes in the magnetic field amplitude, and this behavior is maintained even when a large amplitude magnetic field is applied. This fact means that the high magnetic field sensitivity of the synchronized readout [43] is, in principle, sustained over a wide dynamic range. Thus we believe that this method is particularly suitable for physical property measurements using NVCs. We give two specific examples of its applications. One is the precise measurement of minute stray field. In recent years, atomically thin layered materials [60–62] have been studied extensively, and our scheme applies to the precise measurement of various sorts of magnetization (i.e., ferromagnetism, anti-ferromagnetism, and diamagnetism) of these materials. The other is its application to spin glass [63,64], a representative of systems where fluctuations play an essential role. Our technique is critical in understanding magnetic fluctuations near the spin-glass transition through quantitative measurements of the frequency spectrum of the complex susceptibility.

ACKNOWLEDGMENTS

We thank Takashi Oka and Naoto Tsuji for a helpful discussion and Takuya Isogawa for assistance in early experiments. This work was supported by the Forefront Physics and Mathematics Program to Drive Transformation (FoPM), a World-leading Innovative Graduate Study (WINGS) Program, the University of Tokyo, Grants-in-Aid for Scientific Research Grants No. JP19H00656, JP19H05826, JP20K22325, JP22K03524, JP18H01502, JP22H01558, and JP19H02547, and by Q-LEAP (Grant No. JPMXS0118067395), and the Center for Spintronics Research Network, Keio University.

APPENDIX A: UNDERSAMPLING

We explain why the target ac field frequency (500.1 kHz) is different from the measured frequency of harmonics (multiples of 100 Hz). We used a sequence whose total duration t_L is 20 µs, including initialization, pulse manipulation, and readout. In this scope, since the measurement interval is longer than the period of the target ac field, the frequency of the signal should stroboscopically get undersampled below the Nyquist frequency $\omega_{\mathrm{Ny}} = \pi/t_L$. In the experiment, the detected frequency $\omega_{\mathrm{ac}}^{\mathrm{Ny}}$ should take the value

$$\omega_{\mathrm{ac}}^{\mathrm{Ny}} = \omega_{\mathrm{ac}} - M\omega_{\mathrm{Ny}}, \quad \text{where } M = \left\lfloor \frac{\omega_{\mathrm{ac}}}{\omega_{\mathrm{Ny}}} \right\rfloor. \tag{A1}$$

The peaks of the general harmonic signal should therefore appear at multiples of 100 Hz [= 500.1 kHz − 20 × 25 kHz (= $1/(2 \times 20)\ \mu\mathrm{s}^{-1}$)].

APPENDIX B: PROCESSING OF DFT SIGNALS

We explain the procedure to extract the amplitude of the DFT peaks. We fit the DFT spectrum, taking into account that the peaks of the data have a finite width. We consider that the measurement time window is finite ($t \in [0, T_{\mathrm{tot}}]$, where T_{tot} is the total duration of synchronized readout). We assume the time- series data take the following simplified form:

$$p(t) = Ae^{i(\omega t+\phi)}, \quad t \in [0, T_{\mathrm{tot}}],\ A, \phi \in \mathbb{R}. \tag{B1}$$

This signal can be Fourier transformed as

$$\begin{aligned}\mathcal{F}[p](\xi) &= \int_0^{T_{\mathrm{tot}}} p(t)e^{-i\xi t}dt \\ &= \frac{AT_{\mathrm{tot}}}{4} \exp(i\phi - i(\xi - \omega)T_{\mathrm{tot}}/2)\mathrm{sinc} \\ &\quad \times [(\xi - \omega)T_{\mathrm{tot}}/2],\end{aligned} \tag{B2}$$

where $\mathrm{sinc}(x) \overset{\mathrm{def}}{=} \sin x/x$. Equation (B2) means that the DFT peak spreads over a finite width in the form of a sinc function. We estimate the DFT peak amplitude by fitting the DFT spectrum with the peak shape represented in Eq. (B2).

Figure 8(a) shows the intensity plot obtained using the above method [the same as Fig. 7(a)]. On the other hand, Fig. 8(b) shows the plot obtained simply by extracting the data at the frequency index closest to the kth peak frequency in the DFT spectrum. In Fig. 8(a) a smooth image is obtained, but in Fig. 8(b) there is an artifact where the peak amplitude becomes smaller in a certain period over k. This is an artifact due to the mismatch between the exact peak frequency and the frequency point of the DFT spectrum limited by the frequency resolution $1/T_{\mathrm{tot}}$. The method described above allows accurate determination of the peak amplitude.

After obtaining the DFT peak values, we normalize the time-series data obtained from the synchronized readout for quantitative comparisons with theoretical models. Using the photoluminescence intensity I_0 (count per second) of the $m_S = 0$ state and I_1 (count per second) of the $m_S = -1$ state at the NVC as reference data, we normalize the DFT amplitudes (count) to the dimensionless value of A_k [44]. Specifically, the conversion of the scaling is given as

$$(\text{DFT Amp.}) = A_k N_{\mathrm{seq}}(I_0 - I_1)t_{\mathrm{read}}/2, \tag{B3}$$

where t_{read} is the readout duration (in seconds) and N_{seq} is the total number of CP sequence repetitions.

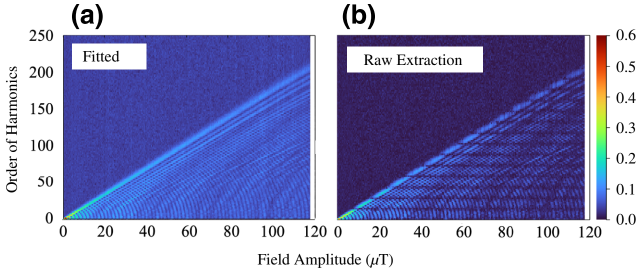

FIG. 8. Intensity map of the DFT peak amplitude. (a) Analyzed result with our fitting method [the same as shown in Fig. 7(a)]. (b) The peak amplitude of the closest frequency point for the kth harmonic.

APPENDIX C: EFFECT OF THE PULSE ERROR AND FINITE PULSE DURATION

We consider the effects of finite pulse duration. First, we consider the pulse error in the $\pi/2$ pulse. When the rotation angle of the pulse is $\pi/2 + \epsilon$, Eq. (30) is rewritten as

$$P_0 \approx \frac{1}{2}(1 + \sin\phi_{\mathrm{acq}} - \epsilon\cos\phi_{\mathrm{acq}}). \tag{C1}$$

Compared to Eq. (30), the pulse error occurs as a cosine term. This term appears as an effect that produces even-order harmonics of the DFT spectrum of the synchronized readout [see Fig. 7(a)].

Next, we consider the effects of finite pulse duration and error in π pulses. Since these effects can produce a variety of effects [14,53–56], we numerically investigate the situation to reproduce experimental observation. Specifically, we solve the time-dependent Schrödinger equation Eq. (1) of the total Hamiltonian $\hat{H}(t) = \hat{H}^{\mathrm{ac}}(t) + \hat{H}^{\mathrm{CP}}(t)$ [Eq. (19)] with finite duration using the adaptive-step Runge-Kutta method. All parameters including pulse phase cycle (XY8) of the Hamiltonian are based on experimental data except the true Rabi frequency. We show the results of these numerical simulations in Fig. 7.

---

[1] J. H. Shirley, Solution of the Schrödinger equation with a Hamiltonian periodic in time, Phys. Rev. **138**, B979 (1965).

[2] H. Sambe, Steady states and quasienergies of a quantum-mechanical system in an oscillating field, Phys. Rev. A **7**, 2203 (1973).

[3] T. Oka and H. Aoki, Photovoltaic Hall effect in graphene, Phys. Rev. B **79**, 081406 (2009).

[4] D. Malz and A. Smith, Topological Two-Dimensional Floquet Lattice on a Single Superconducting Qubit, Phys. Rev. Lett. **126**, 163602 (2021).

[5] I. Martin, G. Refael, and B. Halperin, Topological Frequency Conversion in Strongly Driven Quantum Systems, Phys. Rev. X **7**, 041008 (2017).

[6] A. Eckardt, Colloquium: Atomic quantum gases in periodically driven optical lattices, Rev. Mod. Phys. **89**, 011004 (2017).

[7] C. Weitenberg and J. Simonet, Tailoring quantum gases by Floquet engineering, Nat. Phys. **17**, 1342 (2021).

[8] T. Oka and S. Kitamura, Floquet engineering of quantum materials, Annu. Rev. Condens. Matter Phys. **10**, 387 (2019).

[9] D. M. Lukin, A. D. White, R. Trivedi, M. A. Guidry, N. Morioka, C. Babin, Ö. O. Soykal, J. Ul-Hassan, N. T. Son, T. Ohshima, P. K. Vasireddy, M. H. Nasr, S. Sun, J.-P. W. MacLean, C. Dory, E. A. Nanni, J. Wrachtrup, F. Kaiser, and J. Vučković, Spectrally reconfigurable quantum emitters enabled by optimized fast modulation, npj Quantum Inf. **6**, 80 (2020).

[10] U. Haeberlen and J. S. Waugh, Coherent averaging effects in magnetic resonance, Phys. Rev. **175**, 453 (1968).

[11] J. Choi, H. Zhou, H. S. Knowles, R. Landig, S. Choi, and M. D. Lukin, Robust Dynamic Hamiltonian Engineering of Many-Body Spin Systems, Phys. Rev. X **10**, 031002 (2020).

[12] S. Choi, J. Choi, R. Landig, G. Kucsko, H. Zhou, J. Isoya, F. Jelezko, S. Onoda, H. Sumiya, V. Khemani, C. von Keyserlingk, N. Y. Yao, E. Demler, and M. D. Lukin, Observation of discrete time-crystalline order in a disordered dipolar many-body system, Nature **543**, 221 (2017).

[13] J. Randall, C. E. Bradley, F. V. van der Gronden, A. Galicia, M. H. Abobeih, M. Markham, D. J. Twitchen, F. Machado, N. Y. Yao, and T. H. Taminiau, Many-body–localized discrete time crystal with a programmable spin-based quantum simulator, Science **374**, 1474 (2021).

[14] H. Zhou, J. Choi, S. Choi, R. Landig, A. M. Douglas, J. Isoya, F. Jelezko, S. Onoda, H. Sumiya, P. Cappellaro, H. S. Knowles, H. Park, and M. D. Lukin, Quantum Metrology with Strongly Interacting Spin Systems, Phys. Rev. X **10**, 031003 (2020).

[15] J. Zhang, P. W. Hess, A. Kyprianidis, P. Becker, A. Lee, J. Smith, G. Pagano, I. D. Potirniche, A. C. Potter, A. Vishwanath, N. Y. Yao, and C. Monroe, Observation of a discrete time crystal, Nature **543**, 217 (2017).

[16] W. Beatrez, O. Janes, A. Akkiraju, A. Pillai, A. Oddo, P. Reshetikhin, E. Druga, M. McAllister, M. Elo, B. Gilbert, D. Suter, and A. Ajoy, Floquet Prethermalization with Lifetime Exceeding 90 s in a Bulk Hyperpolarized Solid, Phys. Rev. Lett. **127**, 170603 (2021).

[17] G. de Lange, D. Ristè, V. V. Dobrovitski, and R. Hanson, Single-Spin Magnetometry with Multipulse Sensing Sequences, Phys. Rev. Lett. **106**, 080802 (2011).

[18] J. E. Lang, R. B. Liu, and T. S. Monteiro, Dynamical-Decoupling-Based Quantum Sensing: Floquet Spectroscopy, Phys. Rev. X **5**, 041016 (2015).

[19] J. Meinel, V. Vorobyov, B. Yavkin, D. Dasari, H. Sumiya, S. Onoda, J. Isoya, and J. Wrachtrup, Heterodyne sensing of microwaves with a quantum sensor, Nat. Commun. **12**, 2737 (2021).

[20] S. Ashhab, J. R. Johansson, A. M. Zagoskin, and F. Nori, Two-level systems driven by large-amplitude fields, Phys. Rev. A **75**, 063414 (2007).

[21] G. D. Fuchs, V. V. Dobrovitski, D. M. Toyli, F. J. Heremans, and D. D. Awschalom, Gigahertz dynamics of a strongly driven single quantum spin, Science **326**, 1520 (2009).

[22] J. Scheuer, X. Kong, R. S. Said, J. Chen, A. Kurz, L. Marseglia, J. Du, P. R. Hemmer, S. Montangero, T. Calarco, B. Naydenov, and F. Jelezko, Precise qubit control beyond the rotating wave approximation, New J. Phys. **16**, 093022 (2014).

[23] K. R. K. Rao and D. Suter, Nonlinear dynamics of a two-level system of a single spin driven beyond the rotating-wave approximation, Phys. Rev. A **95**, 053804 (2017).

[24] G. Wang, Y.-X. Liu, and P. Cappellaro, Observation of the high-order mollow triplet by quantum mode control with concatenated continuous driving, Phys. Rev. A **103**, 022415 (2021).

[25] C. Deng, J.-L. Orgiazzi, F. Shen, S. Ashhab, and A. Lupascu, Observation of Floquet States in a Strongly Driven Artificial Atom, Phys. Rev. Lett. **115**, 133601 (2015).

[26] K. Dai, H. Wu, P. Zhao, M. Li, Q. Liu, G. Xue, X. Tan, H. Yu, and Y. Yu, Quantum simulation of the general semi-classical Rabi model in regimes of arbitrarily strong driving, Appl. Phys. Lett. **111**, 242601 (2017).

[27] S. Saito, T. Meno, M. Ueda, H. Tanaka, K. Semba, and H. Takayanagi, Parametric Control of a Superconducting Flux Qubit, Phys. Rev. Lett. **96**, 107001 (2006).

[28] W. D. Oliver, Y. Yu, J. C. Lee, K. K. Berggren, L. S. Levitov, and T. P. Orlando, Mach-zehnder interferometry in a strongly driven superconducting qubit, Science **310**, 1653 (2005).

[29] D. M. Berns, W. D. Oliver, S. O. Valenzuela, A. V. Shytov, K. K. Berggren, L. S. Levitov, and T. P. Orlando, Coherent Quasiclassical Dynamics of a Persistent Current Qubit, Phys. Rev. Lett. **97**, 150502 (2006).

[30] D. M. Berns, M. S. Rudner, S. O. Valenzuela, K. K. Berggren, W. D. Oliver, L. S. Levitov, and T. P. Orlando, Amplitude spectroscopy of a solid-state artificial atom, Nature **455**, 51 (2008).

[31] S. Kotler, N. Akerman, Y. Glickman, and R. Ozeri, Nonlinear Single-Spin Spectrum Analyzer, Phys. Rev. Lett. **110**, 110503 (2013).

[32] J. Zopes, K. Sasaki, K. S. Cujia, J. M. Boss, K. Chang, T. F. Segawa, K. M. Itoh, and C. L. Degen, High-resolution Quantum Sensing with Shaped Control Pulses, Phys. Rev. Lett. **119**, 260501 (2017).

[33] T. Niemczyk, F. Deppe, H. Huebl, E. P. Menzel, F. Hocke, M. J. Schwarz, J. J. Garcia-Ripoll, D. Zueco, T. Hümmer, E. Solano, A. Marx, and R. Gross, Circuit quantum electrodynamics in the ultrastrong-coupling regime, Nat. Phys. **6**, 772 (2010).

[34] P. Forn-Díaz, J. Lisenfeld, D. Marcos, J. J. García-Ripoll, E. Solano, C. J. P. M. Harmans, and J. E. Mooij, Observation of the Bloch-Siegert Shift in a Qubit-Oscillator System in the Ultrastrong Coupling Regime, Phys. Rev. Lett. **105**, 237001 (2010).

[35] F. Yoshihara, T. Fuse, S. Ashhab, K. Kakuyanagi, S. Saito, and K. Semba, Superconducting qubit–oscillator circuit beyond the ultrastrong-coupling regime, Nat. Phys. **13**, 44 (2017).

[36] F. Yoshihara, T. Fuse, S. Ashhab, K. Kakuyanagi, S. Saito, and K. Semba, Characteristic spectra of circuit quantum electrodynamics systems from the ultrastrong- to the deep-strong-coupling regime, Phys. Rev. A **95**, 053824 (2017).

[37] F. Yoshihara, T. Fuse, Z. Ao, S. Ashhab, K. Kakuyanagi, S. Saito, T. Aoki, K. Koshino, and K. Semba, Inversion of Qubit Energy Levels in Qubit-Oscillator Circuits in the Deep-Strong-Coupling Regime, Phys. Rev. Lett. **120**, 183601 (2018).

[38] J. R. Maze, P. L. Stanwix, J. S. Hodges, S. Hong, J. M. Taylor, P. Cappellaro, L. Jiang, M. V. G. Dutt, E. Togan, A. S. Zibrov, A. Yacoby, R. L. Walsworth, and M. D. Lukin, Nanoscale magnetic sensing with an individual electronic spin in diamond, Nature **455**, 644 (2008).

[39] L. T. Hall, C. D. Hill, J. H. Cole, and L. C. L. Hollenberg, Ultrasensitive diamond magnetometry using optimal dynamic decoupling, Phys. Rev. B **82**, 045208 (2010).

[40] B. Naydenov, F. Dolde, L. T. Hall, C. Shin, H. Fedder, L. C. L. Hollenberg, F. Jelezko, and J. Wrachtrup, Dynamical decoupling of a single-electron spin at room temperature, Phys. Rev. B **83**, 081201 (2011).

[41] S. Schmitt, T. Gefen, F. M. Stürner, T. Unden, G. Wolff, C. Müller, J. Scheuer, B. Naydenov, M. Markham, S. Pezzagna, J. Meijer, I. Schwarz, M. Plenio, A. Retzker, L. P. Mcguinness, and F. Jelezko, Submillihertz magnetic spectroscopy performed with a nanoscale quantum sensor, Science **356**, 832 (2017).

[42] J. M. Boss, K. S. Cujia, J. Zopes, and C. L. Degen, Quantum sensing with arbitrary frequency resolution, Science **356**, 837 (2017).

[43] D. R. Glenn, D. B. Bucher, J. Lee, M. D. Lukin, H. Park, and R. L. Walsworth, High-resolution magnetic resonance spectroscopy using a solid-state spin sensor, Nature **555**, 351 (2018).

[44] D. Misonou, K. Sasaki, S. Ishizu, Y. Monnai, K. M. Itoh, and E. Abe, Construction and operation of a tabletop system for nanoscale magnetometry with single nitrogen-vacancy centers in diamond, AIP Adv. **10**, 025206 (2020).

[45] C. L. Degen, F. Reinhard, and P. Cappellaro, Quantum sensing, Rev. Mod. Phys. **89**, 035002 (2017).

[46] K. Mizuno, H. Ishiwata, Y. Masuyama, T. Iwasaki, and M. Hatano, Simultaneous wide-field imaging of phase and magnitude of ac magnetic signal using diamond quantum magnetometry, Sci. Rep. **10**, 11611 (2020).

[47] M. S. J. Barson, L. M. Oberg, L. P. Mcguinness, A. Denisenko, N. B. Manson, J. Wrachtrup, and M. W. Doherty, Nanoscale vector electric field imaging using a single electron spin, Nano Lett. **21**, 2962 (2021).

[48] A. Stark, N. Aharon, T. Unden, D. Louzon, A. Huck, A. Retzker, U. L. Andersen, and F. Jelezko, Narrow-bandwidth sensing of high-frequency fields with continuous dynamical decoupling, Nat. Commun. **8**, 1105 (2017).

[49] S. Saijo, Y. Matsuzaki, S. Saito, T. Yamaguchi, I. Hanano, H. Watanabe, N. Mizuochi, and J. Ishi-Hayase, AC magnetic field sensing using continuous-wave optically detected magnetic resonance of nitrogen-vacancy centers in diamond, Appl. Phys. Lett. **113**, 082405 (2018).

[50] H. Morishita, T. Tashima, D. Mima, H. Kato, T. Makino, S. Yamasaki, M. Fujiwara, and N. Mizuochi, Extension of the coherence time by generating mw dressed states in a single NV centre in diamond, Sci. Rep. **9**, 13318 (2019).

[51] C. Belthangady, N. Bar-Gill, L. M. Pham, K. Arai, D. Le Sage, P. Cappellaro, and R. L. Walsworth, Dressed-State Resonant Coupling between Bright and Dark Spins in Diamond, Phys. Rev. Lett. **110**, 157601 (2013).

[52] A. Stark, N. Aharon, A. Huck, H. A. R. El-Ella, A. Retzker, F. Jelezko, and U. L. Andersen, Clock transition by continuous dynamical decoupling of a three-level system, Sci. Rep. **8**, 14807 (2018).

[53] M. Loretz, J. M. Boss, T. Rosskopf, H. J. Mamin, D. Rugar, and C. L. Degen, Spurious Harmonic Response of Multipulse Quantum Sensing Sequences, Phys. Rev. X **5**, 021009 (2015).

[54] J. M. Boss, K. Chang, J. Armijo, K. Cujia, T. Rosskopf, J. R. Maze, and C. L. Degen, One- and Two-Dimensional Nuclear Magnetic Resonance Spectroscopy with a Diamond Quantum Sensor, Phys. Rev. Lett. **116**, 197601 (2016).

[55] T. Ishikawa, A. Yoshizawa, Y. Mawatari, S. Kashiwaya, and H. Watanabe, Finite-pulse-width effect on quantum sensing for an asynchronous alternating-current magnetic field to dynamical decoupling sequences, AIP Adv. **9**, 075013 (2019).

[56] J. E. Lang, J. Casanova, Z.-Y. Wang, M. B. Plenio, and T. S. Monteiro, Enhanced Resolution in Nanoscale NMR via Quantum Sensing with Pulses of Finite Duration, Phys. Rev. Appl. **7**, 054009 (2017).

[57] M. Pfender, P. Wang, H. Sumiya, S. Onoda, W. Yang, D. B. R. Dasari, P. Neumann, X.-Y. Pan, J. Isoya, R.-B. Liu, and J. Wrachtrup, High-resolution spectroscopy of single nuclear spins via sequential weak measurements, Nat. Commun. **10**, 594 (2019).

[58] K. S. Cujia, J. M. Boss, K. Herb, J. Zopes, and C. L. Degen, Tracking the precession of single nuclear spins by weak measurements, Nature **571**, 230 (2019).

[59] H. Keßler, P. Kongkhambut, C. Georges, L. Mathey, J. G. Cosme, and A. Hemmerich, Observation of a Dissipative Time Crystal, Phys. Rev. Lett. **127**, 043602 (2021).

[60] S. Zhang, R. Xu, N. Luo, and X. Zou, Two-dimensional magnetic materials: Structures, properties and external controls, Nanoscale **13**, 1398 (2021).

[61] X. Jiang, Q. Liu, J. Xing, N. Liu, Y. Guo, Z. Liu, and J. Zhao, Recent progress on 2D magnets: Fundamental mechanism, structural design and modification, Appl. Phys. Rev. **8**, 031305 (2021).

[62] K. F. Mak, J. Shan, and D. C. Ralph, Probing and controlling magnetic states in 2D layered magnetic materials, Nat. Rev. Phys. **1**, 646 (2019).

[63] K. Binder and A. P. Young, Spin glasses: Experimental facts, theoretical concepts, and open questions, Rev. Mod. Phys. **58**, 801 (1986).

[64] H. Taniguchi, M. Watanabe, T. Ibe, M. Tokuda, T. Arakawa, T. Taniguchi, B. Gu, T. Ziman, S. Maekawa, K. Kobayashi, and Y. Niimi, Spin treacle in a frustrated magnet observed with spin current, Phys. Rev. B **102**, 094405 (2020).